J. Fluid Mech. (2024), *vol*. 984, A60, doi:10.1017/jfm.2024.266

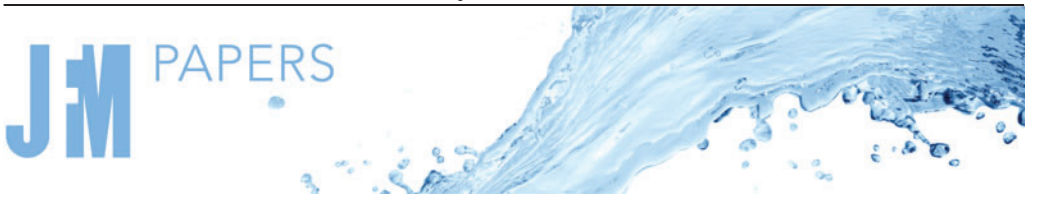

Formation and evolution of laminar thermal structures: correlation to the thermal boundary layer and effects of heating time

Pei-Jiang Qin[1,2], Yu-Yang Hou[2], Ji-Dong He[2,3], Ping Wei[4] and Shi-Di Huang[2,3,†]

[1]School of Astronautics, Harbin Institute of Technology, Harbin 150001, PR China

[2]Department of Mechanics and Aerospace Engineering and Center for Complex Flows and Soft Matter Research, Southern University of Science and Technology, Shenzhen 518055, PR China

[3]Guangdong Provincial Key Laboratory of Turbulence Research and Applications, Southern University of Science and Technology, Shenzhen 518055, PR China

[4]School of Aerospace Engineering and Applied Mechanics, Tongji University, Shanghai 200092, PR China

(Received 17 August 2023; revised 27 January 2024; accepted 9 March 2024)

We report an experimental study of the formation and evolution of laminar thermal structures generated by a small heat source, with a focus on their correlation to the thermal boundary layer and effects of heating time t_{heat}. The experiments are performed over the flux Rayleigh number (Ra_f) range $2.1 \times 10^6 \leq Ra_f \leq 3.6 \times 10^7$ and the Prandtl number (Pr) range $28.6 \leq Pr \leq 904.7$. The corresponding Rayleigh number ($Ra = t_{heat}\, Ra_f/\tau_0\, Pr$) range is $900 \leq Ra \leq 4 \times 10^4$, where τ_0 is a diffusion time scale. For thermal structures generated by continuous heating (i.e. starting plumes), their formation process exists three characteristic times that are well reflected by changes in the thermal boundary layer thickness. These characteristic times, denoted as t_{emit}, $t_{recover}$ and t_{static}, correspond to the moments when the plume emission begins and completes, and when the thermal boundary layer becomes quasi-static, respectively. Their Ra_f–Pr dependencies are found to be $t_{emit}/\tau_0 \sim Ra_f^{-0.41}\, Pr^{0.41}$, $t_{recover}/\tau_0 \sim Ra_f^{-0.48}\, Pr^{0.48}$ and $t_{static}/\tau_0 \sim Ra_f^{-0.49}\, Pr^{0.33}$, respectively. Thermal structures generated by finite t_{heat} exhibit similar evolution dynamics once $t_{heat} \geq t_{emit}$, with the accelerating stage behaving like starting plumes and the decay stage like thermals (i.e. a finite amount of buoyant fluids). It is further found that their maximum rising velocity experiences a transition in the Ra-dependence from Ra to $(Ra \ln Ra)^{0.5}$ at $Ra \simeq 6000$; and their maximum acceleration reaches the value of starting plumes at $t_{heat} \simeq t_{recover}$, and remains unchanged for larger t_{heat}. In particular, the maximum rising velocity for the cases with $t_{heat} = t_{recover}$ follows

† Email address for correspondence: huangsd@sustech.edu.cn

a scaling relation $Ra_f^{0.37}\,Pr^{-0.37}$, in contrast to the relation $Ra_f^{0.48}\,Pr^{-0.48}$ for starting plumes. This study provides a more comprehensive understanding of laminar thermal structures, which are relevant to a range of processes in nature and laboratory systems such as Rayleigh–Bénard convection.

Key words: plumes/thermals

1. Introduction

Convection flows generated by localized heat sources are an important class of fundamental problems in fluid dynamics, which are relevant to many phenomena in nature and in industrial applications (Turner 1969; Jellinek & Manga 2004; Woods 2010). Depending on how the heat is supplied, the generated thermal structures in these flows can be classified into mainly two types: thermals and plumes (Turner 1969). Thermals are used to describe a finite amount of buoyant fluids that are released suddenly and then evolve freely without connection to the heat source. For plumes, they refer to steady convection flows rising from the heat source with continuous heat supply. In particular, before plumes reach the steady state, they are called starting plumes, which consist of a mushroom-shaped head and a long tail that are similar to a thermal and a plume, respectively (Turner 1962; Shlien 1976).

In real situations, these thermal structures can be either laminar or turbulent, and they can be found in a wide variety of flow scenarios, such as in a stratified fluid environment and in a turbulent shear flow (Turner 1973; Helfrich 1994; Bhamidipati & Woods 2017; Bhaganagar & Bhimireddy 2020; Orlandi & Carnevale 2020). In this study, we focus on the laminar case in a homogeneous stationary fluid layer. Although this simple flow scenario has received extensive studies over the years, there remain some open issues to be addressed.

The first issue that we aim to address in this study is related to plumes. Early studies of plumes focused on their evolution process, which was pioneered by the theoretical work of Batchelor (1954). Based on dimensional analysis and self-similarity theory, Batchelor (1954) derived the similarity solutions of various characteristics of plumes during the evolution process, including the ascent height, the diameter and the velocity/temperature profile. These similarity solutions have been proved by theoretical analysis, numerical simulations and experimental observations (Yih 1952; Fujii 1963; Gebhart, Pera & Schorr 1970; Pera & Gebhart 1971; Fujii, Morioka & Uehara 1973; Shlien & Boxman 1979; Worster 1986). Moreover, it is found that the scaling relations developed for plumes are also applicable to the heads of starting plumes over a wide range of Prandtl numbers (characterizing the fluid properties) and even fluids with a strong temperature-dependent viscosity (Shlien 1976, 1979; Moses *et al.* 1991; Moses, Zocchi & Libchaberii 1993; Kaminski & Jaupart 2003; Davaille *et al.* 2011).

Compared to the considerable efforts on the evolution process of plumes (including the starting plumes), their formation behaviour near the heat source has been less explored. As far as we know, there are limited experimental studies trying to determine the time required for the build-up of plumes by watching the convection patterns (Vest & Lawson 1972; Davaille & Vatteville 2005). Although their results are in agreement with the onset time of thermal boundary layer instability (Howard 1966), the correlation between the formation process of plumes and the development of the thermal boundary layer has not been examined quantitatively in detail. This motivates us to perform a series of experiments to address this issue, which is one main objective of the present study.

Conducting a detailed investigation of the formation process of plumes is also insightful for the study of turbulent Rayleigh–Bénard convection (Ahlers, Grossmann & Lohse 2009). In this canonical convection system, the formation and emission of plumes is not only due to the thermal boundary layer instability (Malkus 1954; Howard 1966), but also subject to the perturbation from turbulent flow (Kadanoff 2001; Lithgow-Bertelloni *et al.* 2001; Funfschilling & Ahlers 2004; Xi, Lam & Xia 2004; Zhou *et al.* 2010; Shishkina *et al.* 2015; Wang *et al.* 2018; Xu *et al.* 2021). Briefly, rather than being fully developed and then emitting from the thermal boundary layer, some 'plumes' could be taken away by the turbulent flow at early stages of their formation process. (These 'plumes' are different from the standard definitions of plumes and thermals, so we simply call them thermal structures hereafter.) Thermal structures emitted at different stages of the formation process can be viewed as fluid parcels being heated inside the boundary layer with different heating times and thus contain different amounts of buoyancy. This motivates us to raise the second issue of the present study: how would the properties of thermal structures be influenced by the heating time (or equivalently, the total buoyancy supplied to them)?

The answer to the question above is also relevant to the study of thermals. In contrast to plumes and starting plumes, thermals are disconnected from the heat source, so they have a fixed amount of buoyancy that is quantified by the Rayleigh number Ra. Early theoretical work by Morton (1960) suggested that the rising velocity of thermals depends on Ra linearly when $Ra \ll 1$. For the situation with $Ra \gg 1$, Shlien and his co-worker found in their experiments that the rising velocity of thermals scales with Ra as $Ra^{0.9}$ over a limited range $3200 \leq Ra \leq 9600$ (Shlien & Thompson 1975; Shlien 1976). By extending Ra to a wider range, from 250 to 25 000, Griffiths (1986) found a different scaling $Ra^{3/4}$ in his experiment, and he developed a theoretical model for thermals at large Ra to explain this finding. However, the Griffiths model was questioned by Whittaker & Lister (2008) recently. By assuming that most of the buoyancy is spread into the wake flow in the tail rather than remaining in the head of thermals, Whittaker & Lister (2008) predicted that the rising velocity of thermals at large Ra follows a scaling $(Ra \ln Ra)^{0.5}$, which was supported by their numerical results. Thus the discrepancy between these studies of thermals is a puzzle. According to Whittaker & Lister (2008), there could be several factors accounting for the discrepancy, such as the initial transient behaviour, the boundary conditions, and the properties of the fluids used. While a later numerical study (Peng & Lister 2014) supported the model proposed by Whittaker & Lister (2008), the experimental evidence for the existence of the scaling $(Ra \ln Ra)^{0.5}$ is still absent. Moreover, if the Griffiths model is incorrect, then it is unclear why his theoretical prediction matches well with his experimental results. Therefore, new experiments are required to solve this issue.

In this study, we performed a series of experiments to investigate the properties of laminar thermal structures generated by a small heat source. Special attention has been paid to the correlation between the plume formation and the thermal boundary layer development. Four distinct stages separated by three characteristic times were observed during the plume formation process. Based on these characteristic times, we have made a detailed investigation of thermal structures generated by finite heating time, which contain finite amounts of buoyancy and thus can be viewed as thermals (Shlien 1976; Whittaker & Lister 2008). By varying the heating time and thus the buoyancy strength (Ra), we found that the Ra-dependent scaling of the rising velocity of thermals show a crossover from Ra to $(Ra \ln Ra)^{0.5}$, resulting in an effective scaling $Ra^{0.78}$ over the Ra range explored ($900 \leq Ra \leq 4 \times 10^4$). This finding provides an experimental explanation for the aforementioned puzzle about thermals.

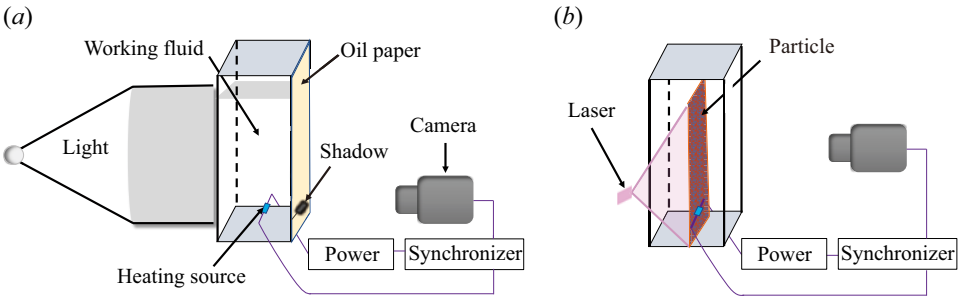

Figure 1. Schematic diagrams of the experimental set-up and techniques used in the present study: (*a*) shadowgraph; (*b*) particle image velocimetry. See text for a detailed description.

The remainder of this paper is organized as follows. Section 2 introduces details of the experimental apparatus and the techniques used. The experimental results are presented in § 3. We first show the plume formation process and its correlation to thermal boundary layer development in § 3.1. The effects of heating time are discussed in § 3.2, followed by a detailed investigation of thermal structures generated by a critical heating time in § 3.3. Finally, the main findings are summarized in § 4.

2. Experimental apparatus, equipment and methods

2.1. *Apparatus and key parameters*

According to previous studies (Moses *et al.* 1993; Kaminski & Jaupart 2003; Bond & Johari 2005; Whittaker & Lister 2008; van Keken, Davaille & Vatteville 2013; Kondrashov, Sboev & Dunaev 2016*a*; Kondrashov, Sboev & Rybkin 2016*b*), the properties of thermal structures generated by a small heat source could be affected by several factors in laboratory experiments. These factors include mainly the dimensions and geometries of the heat source and the tank, the boundary conditions, the properties of the fluid, and the leakage of the heating power. These factors had been considered in our experiments to minimize their influence as much as possible.

As illustrated in figure 1, the experiments were conducted in a Perspex tank of dimensions 150 mm × 100 mm × 350 mm (length × width × height). A lid was closely fitted to the tank's top to prevent free surface effects as well as the influence of evaporative convection (Hay & Papalexandris 2020). Silicone oil was selected as the working fluid because of its weak temperature-dependent viscosity. Five kinds of silicone oil (KF-96 series, Shin-Etsu Chemical Co. Ltd) were used in the present study, resulting in Prandtl number $Pr = \upsilon/\kappa$ range $28.6 \leq Pr \leq 904.7$. Here, υ and κ are the kinematic viscosity and thermal diffusivity of the silicone oil, detailed values of which are shown in table 1. Other relevant fluid properties, such as density ρ, thermal capacity c_p and thermal expansion coefficient α, are also listed in table 1. The values of these fluid properties are provided by Shin-Etsu Chemical Co. Ltd (available upon request from https://www.shinetsusilicone-global.com). In addition, their reliability has been checked by independent measurements from another commercial company that offers analysing and testing services for diverse materials (NETZSCH, https://analyzing-testing.netzsch.com/en).

A commercial resistor (Tokyo Koon Co. Ltd) with a cylindrical shape (length 6.0 mm, diameter 1.8 mm) was used as the heat source. It was much smaller than the tank and located at a distance 60 mm above the tank's bottom, so the effects of the walls are negligible. The resistor is a metal-film resistor supported by a ceramic cylinder inside,

Silicone oil	Pr	ρ	c_p	υ ($\times 10^{-6}$)	κ ($\times 10^{-8}$)	α ($\times 10^{-3}$)	τ_0	u_0 ($\times 10^{-5}$)	a_0 ($\times 10^{-6}$)
2cs	28.6	873.0	1887	2.0	7.00	1.24	38.4	4.27	1.11
5cs	68.6	915.0	1830	5.0	7.29	1.09	36.9	4.45	1.20
20cs	202.7	950.0	1728	20.0	9.87	1.04	27.3	6.02	2.21
50cs	480.0	960.0	1634	50.0	10.42	0.96	25.9	6.34	2.45
100cs	904.7	965.0	1521	100.0	11.05	0.95	24.2	6.77	2.79

Table 1. Physical properties (at 25.0 °C) of silicone oils used in the present study, and the corresponding Prandtl numbers. Here, ρ (kg m^{-3}), c_p (J kg^{-1} K^{-1}), υ (m^2 s^{-1}), κ (m^2 s^{-1}) and α (K^{-1}) are the density, thermal capacity, kinematic viscosity, thermal diffusivity and thermal expansion coefficient, respectively. The corresponding diffusive quantities based on the effective length r_0 of the heat source, including time $\tau_0 = r_0^2/\kappa$ (s), velocity $u_0 = r_0/\tau_0$ (m s^{-1}), and acceleration $a_0 = u_0/\tau_0$ (m s^{-2}), are also listed for reference.

so it has a fast thermal response time. For example, by putting a thermistor (model TE-GAG22K7MCD419, diameter ∼0.3 mm) on the resistor's surface, it was found that the thermal response time of the resistor was at most 0.25 s for the measurements made at $Pr = 904.7$, the influence of which on the characteristic times of thermal structures (presented in § 3.1) is no more than 3 %. The resistor's resistance has a relationship with the temperature as $R(\Omega) = 220.6 - 0.048 \times T\,(^\circ\mathrm{C})$, and its variation due to the temperature change was smaller than 2 % in the present study. The resistor was connected to a DC power supply (XDL 56-4P, Sorensen Co. Ltd) under constant voltage mode with accuracy 0.1 %, so the variation of heating power during the measurement can be ignored.

The heating power P was adjusted over different ranges for different silicone oils. The lowest heating power was determined by the requirement that the generated thermal structures should be well distinguished from the background fluid in the shadowgraph visualization (introduced in § 2.2). The maximum heating power was limited by the boiling points of the silicone oils used. Consequently, the flux Rayleigh number $Ra_f = \alpha g r_0^2 P/\kappa^3 \rho c_p$ (Moses *et al.* 1993) in the present study was restricted to the range of $2.1 \times 10^6 \leq Ra_f \leq 3.6 \times 10^7$. Here, g is the gravitational acceleration, and r_0 is the effective heating length. For the cylindrical resistor used here, r_0 is equal to the radius of a sphere with the same surface area, thus $r_0 = 1.64$ mm. Based on this effective heating length, the corresponding diffusive time, velocity and acceleration can be defined as $\tau_0 = r_0^2/\kappa$, $u_0 = r_0/\tau_0$ and $a_0 = u_0/\tau_0$, respectively. Detailed values of these diffusive quantities are listed in table 1 for reference.

It is worth noting that the resistor can also absorb heat during the experiments, so the actual heating power supplied to the fluid and thus Ra_f could be smaller. To assess the influence of this problem, one can estimate the maximum amount of heat that can be absorbed by the resistor based on its mass (0.028 g) and specific heat capacity (approximately 0.7 J g^{-1} K^{-1}), which is at most 10 % of the total heat supplied during the experiments. Note that this assessment gives an upper limit and has overestimated this problem. According to a previous experimental study of starting plumes (Kaminski & Jaupart 2003), the thermal leakage problem is negligible for $Pr \leq 300$, and is only a small fraction of the total heat for larger Pr. As we will show in § 3.3, the rising velocities of starting plumes obtained in the present study agree well with the results obtained by Kaminski & Jaupart (2003), although a very different heat source (electric coil of diameter 5 mm) and measurement technique (differential interferometry) were used in their experiments. This good agreement supports the findings in the present study not being affected by the thermal leakage problem.

Besides the heating power P, the heating time t_{heat} is another key parameter in the present study. Note that t_{heat} is the time duration for heating power supplied to the fluid, after which the power supply will be turned off. This is different from 'a ramp heating of finite time' considered in a previous study (Jiang *et al.* 2021). To control and vary t_{heat} accurately, the power supply was connected to a programmable function generator. As both the heating power P and the heating time t_{heat} contribute to the total buoyancy contained in thermal structures, the combined effect can be quantified by the Rayleigh number $Ra = \alpha g P t_{heat}/\upsilon\kappa\rho c_p = t_{heat}\, Ra_f/\tau_0\, Pr$ (Batchelor 1954; Morton, Taylor & Turner 1956), which was changed from 900 to 4×10^4 in the present study.

2.2. *Experimental techniques*

Two different experimental techniques were used in the present study, namely the shadowgraph technique (Settles 2001) and particle image velocimetry (PIV) (Raffel *et al.* 2018). The shadowgraph technique schematic diagram is shown in figure 1(*a*). The fluid was illuminated evenly by a home-made parallel light source with the help of a set of collimating lenses. An oil tracing paper was pasted onto the back wall of the tank as the projection screen. Because the density of the hot fluid parcel is smaller than that of the ambient fluid, the light intensity after transmitting through the fluid will become uneven due to the local temperature(density) variation, resulting in a shadow pattern projected on the screen. Therefore, the outline of the shadow pattern can well reflect the position where large temperature contrast lies. By recording a series of shadow images with a digital camera (Nikon D850, 3840 × 2160 pixels, 24 fps), both the development of the thermal boundary layer and the formation of the thermal structure can be revealed simultaneously.

The PIV technique was used to measure the rising velocity of the thermal structure (see figure 1*b*). Because of the low densities of silicone oils, it is not easy to find suitable particles to perform PIV measurements in the present study. We have tried several different kinds of particles, and happened to find that one kind of fluorescent particle, $Eu(TTA)_3phen$ (CAS no. 17904-86-8 series, Tokyo Chemical Industry) can meet our requirements. To be specific, we first used a 20 μm filter to pick out the particles with desirable diameters. Then these particles were added into the silicone oil and stirred by an ultrasonator. After the seeding particles were distributed uniformly in the silicone oil, we left the fluid to rest for 4 hours before starting the PIV measurements. These procedures allow good density matching between the particles and the fluid, so the particles can be suspended in the silicone oil for a long time without visible settling. Depending on the silicone oil used as well as the flow strength, the Stokes number was found to vary from $O(10^{-4})$ to $O(10^{-2})$ in the present study, confirming that the particles can well follow the flow motion.

During the PIV measurements, a continuous laser was used to illuminate the vertical plane across the resistor, then the particle images were acquired with a digital camera (Nikon D850, 3840 × 2160 pixels, 24 fps). The post-process analysis of particle images was carried out by commercial software (Dantec DynamicStudio). Briefly, the adaptive PIV scheme was used to obtain the velocity fields. This scheme can iteratively adjust the size and shape of individual interrogation windows to adapt to local particle concentrations and velocity gradients. The maximum (minimum) interrogation window size was 64 pixels × 64 pixels (32 pixels × 32 pixels), while the grid step size was 16 pixels × 16 pixels. Although the images were acquired at a fixed recording rate of 24 Hz, the actual time delay between a pair of particle images used in the PIV analysis was adjusted according to the characteristic velocities of thermal structures, so that the mean particle

displacements were in an approximate range 4–8 pixels. In order to make an estimation of our PIV measurement errors (Raffel *et al.* 2018), we have performed measurements in quiescent silicone oils without heating power. It was found that the maximum measured velocities in these control experiments ranged from 0.02 to 0.04 mm s^{-1} for different Pr, which are only 1 %–3 % of the smallest characteristic velocities of thermal structures presented in § 3.

To ensure that the image recording started immediately when the power supply was turned on, a synchronizer was used in both the shadowgraph and PIV measurements. For each parameter setting (i.e. the same Ra_f, Pr and t_{heat}), the measurements were repeated 20 times, and the ensemble average results were used for data analysis. The time interval between two successive measurements was approximately 1–2 hours, so that the fluid was allowed to become motionless before the new measurement. The ambient temperature was controlled to be $25 \pm 1\,^{\circ}$C for all the measurements.

2.3. *Comparison of the results from shadowgraph and PIV*

Most previous studies used the shadowgraph technique to measure the characteristic velocity of thermal structures generated by a small heat source (Shlien & Thompson 1975; Shlien 1976; Griffiths 1986; Moses *et al.* 1991, 1993; Kaminski & Jaupart 2003). To check how the PIV results are compared with the data obtained from the shadowgraph technique, we have made some test measurements in this study. Figure 2 shows snapshots of the shadowgraph image and PIV-obtained flow fields of a thermal structure during its evolution process. The control parameters for this case are $Pr = 904.7$, $Ra_f = 6.5 \times 10^6$ and $t_{heat} = 10.6$ s. The results for different techniques were obtained separately but measured at the same moment after the heating power was turned on.

To capture the outline of the thermal structure clearly, the raw shadowgraph image has been subtracted by a background image taken when the heating power was off, and the image contrast has been enhanced by applying appropriate thresholds (Maragatham & Roomi 2015; Zhou *et al.* 2016). With the contrast improvement, it is seen clearly in figure 2(*a*) that the thermal structure has a shape similar to a starting plume, characterized by of a mushroom-like head and a slender tail. From this image, we can determine the upper edge of the thermal structure and thus its ascent height (the black dashed line in figure 2). The rising velocity of the thermal structure can be calculated by taking the time derivative of its ascent height.

We can also obtain the rising velocity of the thermal structure from the PIV results. However, it is not easy to identify the thermal structure from the velocity field shown in figure 2(*b*). Although the black dashed line, corresponding to the upper edge of the thermal structure, seems to go across the location where the vertical velocity's gradient in the y direction is maximal (figure 2*c*), the velocity variation near the sharpest gradient is so strong that small deviations will lead to large uncertainties in determining its position. In addition, there is no clear correlation between the upper edge of the thermal structure and the vorticity field (figure 2*d*). Interestingly, combined with the shadowgraph image, it is seen that the location of the maximum vertical velocity (indicated by the red solid line in figure 2) corresponds to the lower edge of the thermal structure. As the maximum vertical velocity and its location can be determined easily from the PIV field, they are good choices for characterizing the rising velocity and ascent height of the thermal structure.

To compare the results from shadowgraph and PIV quantitatively, we plot in figure 3 the time series of the ascent height and the rising velocity of thermal structures measured at $Pr = 904.7$ for three different Ra_f values. The heating times t_{heat} for these Ra_f were all set

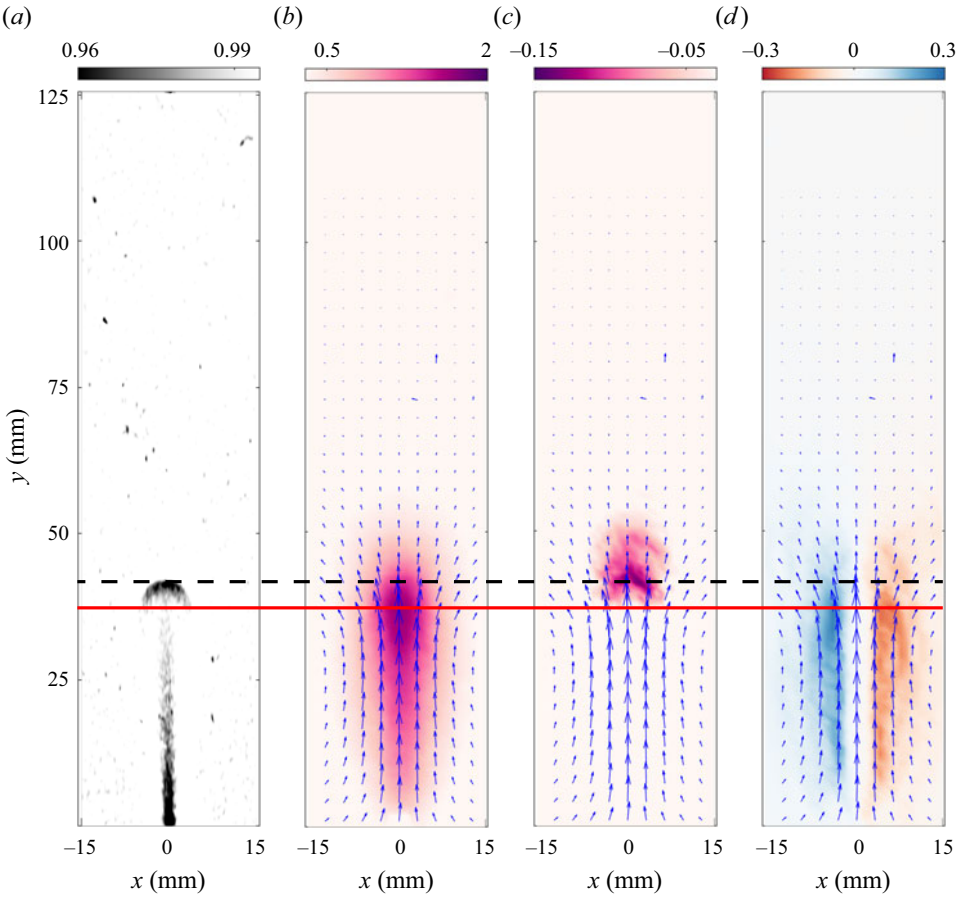

Figure 2. Instantaneous flow fields of a thermal structure during its evolution process. The measurements were made at $Pr = 904.7$ and $Ra_f = 6.5 \times 10^6$, with heating time $t_{heat} = 10.6$ s. (*a*) The shadowgraph image, with the colour reflecting the strength of local temperature variation. (*b–d*) The PIV-obtained results of vertical velocity (mm s^{-1}), vertical velocity's gradient in the y direction (s^{-1}), and vorticity (s^{-1}), respectively. Their magnitudes are indicated by their own colour scales, and the arrows represent the velocity vectors. The dashed black line indicates the ascent height of the thermal structure according to the shadowgraph image, and the red solid line indicates the position of the maximum vertical velocity in the PIV field at the same moment.

to $t_{recover}$, which were different for different Ra_f (see § 3.1 for a detailed explanation). It is seen in figure 3(*a*) that the ascent heights obtained from different methods have a similar evolution trend. Note that the shadowgraph data represent the upper edge of the thermal structure (the black dashed line in figure 2), while the PIV data represent the lower edge of the thermal structure (the red solid line in figure 2). By taking time derivative of the ascent height, we can obtain the Lagrangian velocities of thermal structures. However, taking the time derivative directly will result in a large error, so a Gaussian convolution method was applied to reduce the data noise (Mordant, Crawford & Bodenschatz 2004), which will smooth out some data in the time series. The Lagrangian velocities thus obtained are plotted in figure 3(*b*). It is seen that the results from shadowgraph and PIV, i.e. the Lagrangian velocities of thermal structures at their upper and lower edges, almost fall on top of each other. It is further seen in figures 3(*c*,*d*) that the maximum vertical velocities obtained from the PIV field directly, i.e. the Eulerian vertical velocities of thermal structure

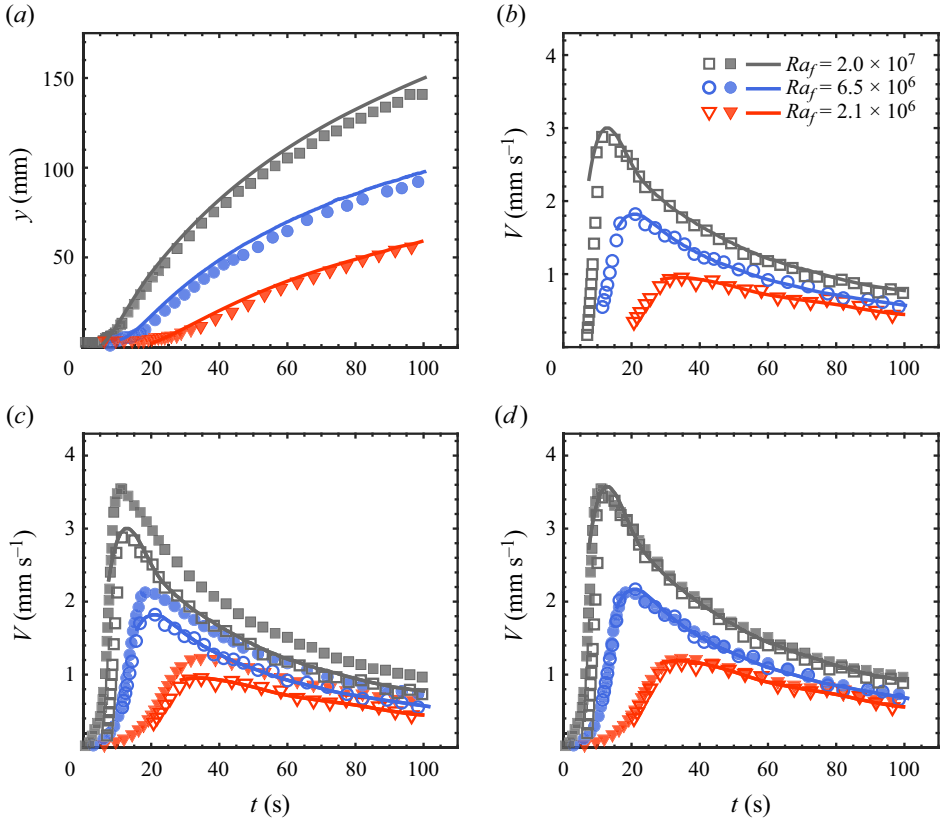

Figure 3. Comparisons of the results obtained from shadowgraph (lines) and PIV (symbols). The measurements were made at $Pr = 904.7$ for three different Ra_f. (*a*) The ascent heights of thermal structures. (*b*) The Lagrangian velocities of thermal structures obtained by taking the time derivative of the data in (*a*). (*c*) The same data as in (*b*), together with the maximum vertical velocities (solid symbols) obtained from the PIV field directly. (*d*) The same data as in (*c*), but the Lagrangian velocities (both lines and open symbols) are multiplied by a factor 1.2 for all Ra_f.

at their lower edge, are in good agreement with the Lagrangian data, differing only by a factor 1.2. This comparison suggests that the results obtained from shadowgraph and PIV are basically consistent and can be used to characterize the properties of thermal structures in the present study.

However, it should be noted that no thermal structure can be identified from the shadowgraph image before its emission from the thermal boundary layer, so there are no shadowgraph data at the very beginning of the time series (see figure 3*a*). Moreover, to obtain the Lagrangian velocities of thermal structures from their ascent heights, further calculation with a Gaussian convolution method is required, which leads to more data loss in the time series (see figure 3*b*). By contrast, the Eulerian vertical velocities of thermal structures can not only be obtained from the maximum vertical velocity in the PIV field directly (without further calculation), but also provide more information on the formation and evolution processes (without data loss). Therefore, in the following sections, we will use the maximum vertical velocities in the PIV fields and their locations to represent the rising velocities and the ascent heights of thermal structures.

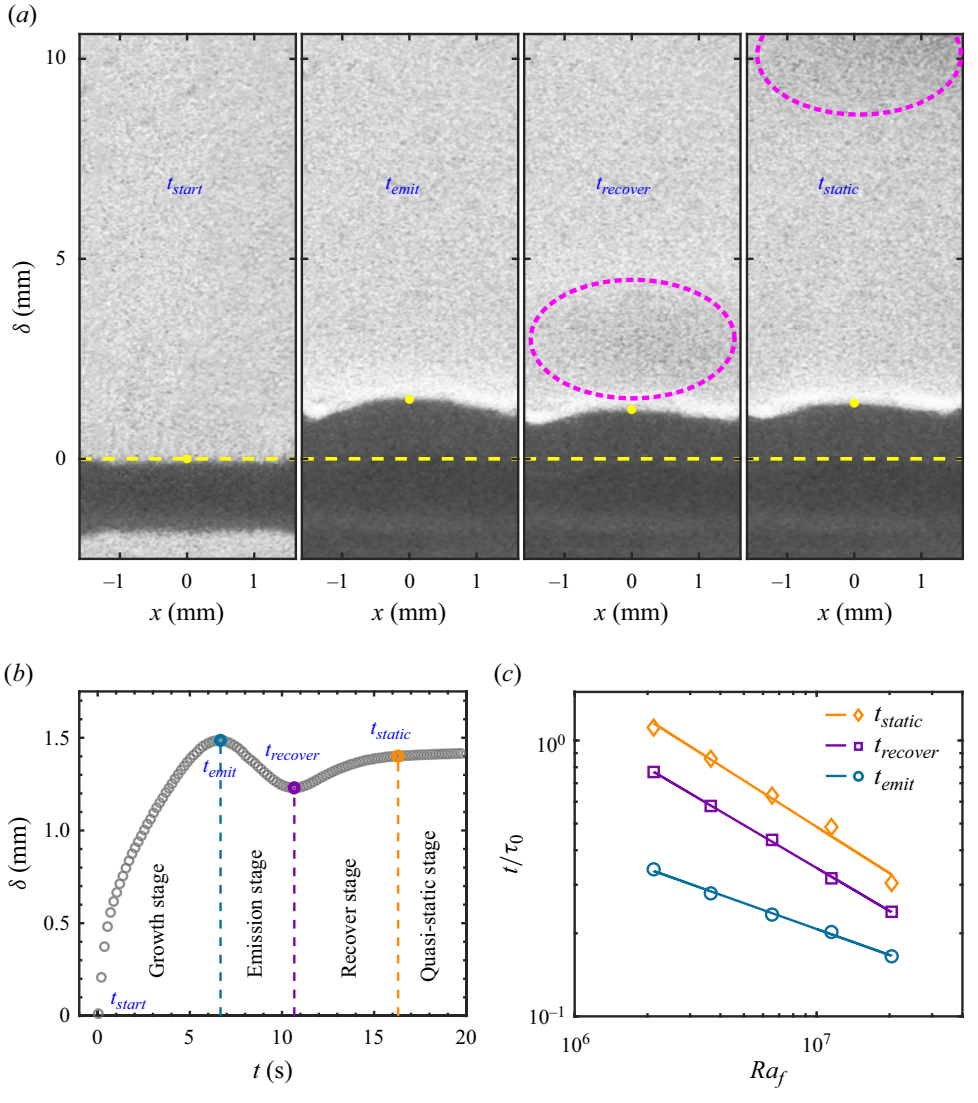

Figure 4. (*a*) Shadowgraph images at four typical moments during the formation of a starting plume at $Pr = 904.7$ and $Ra_f = 6.5 \times 10^6$. The complete process is shown in the supplementary movie available at https://doi.org/10.1017/jfm.2024.266. The pink dashed line highlights the position of the emitted plume. The yellow dashed line and dot represent the top surface of the resistor and the edge of the TBL, respectively, and their vertical distance is used to characterize the thickness δ of the TBL. (*b*) Plot of δ as a function of time after the heating power was turned on, from which four distinct stages separated by three characteristic times can be determined. (*c*) The three characteristic times as functions of Ra_f at $Pr = 904.7$. Here, all the characteristic times have been normalized by the diffusive time $\tau_0 = r_0^2/\kappa$ defined in § 2.1. The solid lines are power-law fits to each data set: $t_{emit}/\tau_0 \sim Ra_f^{-0.31\pm0.01}$, $t_{recover}/\tau_0 \sim Ra_f^{-0.52\pm0.01}$ and $t_{static}/\tau_0 \sim Ra_f^{-0.56\pm0.04}$.

3. Results and discussion

3.1. *Development of the thermal boundary layer and formation of plumes*

In this subsection, we present how the plume formation process is correlated to the development of the thermal boundary layer (TBL). Figure 4(*a*) shows four snapshots of shadowgraph images near the top surface of the heat source (indicated by the yellow

dashed line). The measurement was made at $Pr = 904.7$ and $Ra_f = 6.5 \times 10^6$ with continuous heating, so the generated thermal structure was in the starting stage of a plume, i.e. a starting plume. According to the working principle of shadowgraph technique, the TBL is displayed as a dark strip in these images, and the location with the strongest temperature gradient is the edge of the TBL (indicated by the yellow dots). Therefore, we can determine the thickness δ of the TBL by the vertical distance between the yellow line and the yellow dot. Note that the absolute value of δ is affected by the inevitable optical distortion in the shadowgraph measurements, so we just examine its change with time here.

The δ thus determined as a function of time is plotted in figure 4(*b*). It is seen that the evolution of δ can be divided into four stages: the growth stage, the emission stage, the recover stage and the quasi-static stage. Specifically, after the heating power is turned on at t_{start}, heat is conducted into the fluid and the TBL begins to build up. During the growth stage, the TBL grows in its thickness δ, but remains stable. When δ reaches a critical value at $t = t_{emit}$, a plume starts to emit due to the instability of the TBL. Because some hot fluid parcels inside the TBL are taken away by the plume, the TBL shrinks, and its thickness δ decreases during the emission stage. As time goes by, the head of the plume becomes completely detached from the TBL at $t = t_{recover}$ and its tail appears, indicating the formation of a well-defined starting plume. At this critical moment, δ reaches a local minimum, then the TBL gets into the recover stage. During the recover stage, the TBL grows again gradually thanks to the continuous heating supplied from the heat source, and eventually becomes quasi-static at $t = t_{static}$. In the quasi-static stage, because all the heat supplied is taken away by the convection flow, the TBL becomes stable again and its thickness remains unchanged. It is interesting to note that similar evolution of the TBL thickness (growth–drop–stationary) was observed in some numerical studies of buoyancy-driven flows on a heated horizontal plate (Jiang, Nie & Xu 2019*a*,*b*; Jiang *et al.* 2021). However, these studies did not observe the recover stage as in the present experimental study. Further investigations combined with experiments and simulations are required to find the reason for this difference.

The complete process described above can be found in the supplementary movie, which clearly shows how the plume formation is correlated to the development of the TBL. During this process, three characteristic times are identified, and their Ra_f dependencies are plotted in figure 4(*c*). It is seen that t_{emit}/τ_0, $t_{recover}/\tau_0$ and t_{static}/τ_0 exhibit distinct Ra_f-dependent scaling exponents, being -0.31, -0.52 and -0.56, respectively. The scaling of $t_{recover}/\tau_0$ recalls the study by Moses *et al.* (1993), who predicted that the build-up time for starting plumes follows a relation $t_{build\text{-}up}/\tau_0 \sim Ra_f^{-0.5}\, Pr^{0.5}$.

To compare our results with this theoretical prediction, we plot different characteristic times for all the Pr in figure 5. It is seen that $t_{recover}/\tau_0$ obeys a scaling relation $Ra_f^{-0.48}\, Pr^{0.48}$ for the present parameters explored, which is in good agreement with the theoretical prediction mentioned above. In terms of magnitude, $t_{recover}$ measured directly in the present study is very close to the experimental values of $t_{build\text{-}up}$ reported by Moses *et al.* (1993). However, Moses *et al.* (1993) did not measure $t_{build\text{-}up}$ directly. Instead, they assumed that the starting plume was originated from a 'virtual point source y_{virt}' at $t = 0$, and the plume's ascent height could be described by a function $y = V_{starting}(t - t_{build\text{-}up})$, where $V_{starting}$ is the rising velocity of the starting plume at the steady state. Then $t_{build\text{-}up}$ can be evaluated to be $t_{build\text{-}up} = -y_{virt}/V_{starting}$. Although the result yielded from this estimation ($t_{build\text{-}up}/\tau_0 \sim Ra_f^{-0.46}\, Pr^{0.46}$) is consistent with their theory, the obtained $t_{build\text{-}up}$ is physically ambiguous, and the data plotted in figure 5 are relatively scattered.

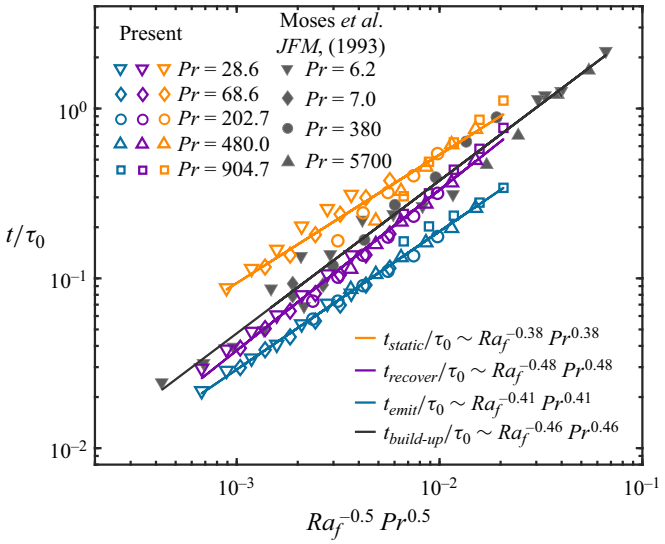

Figure 5. Different normalized characteristic times as functions of $Ra_f^{-0.5}\, Pr^{0.5}$. The solid symbols are the build-up times for starting plumes measured indirectly by Moses *et al.* (1993). The solid lines are the best power-law fits to each data group.

This is in contrast to $t_{recover}$ in the present study, which can be determined precisely thanks to its clear physical meaning as revealed by figure 4.

The physical meaning of t_{emit} is also revealed unambiguously by figure 4. This data group can be fitted by a power law $t_{emit}/\tau_0 \sim Ra_f^{-0.41}\, Pr^{0.41}$. To understand this scaling relation, we note that at the moment of plume emission, the time duration for heating power being supplied to the fluid (i.e. the heating time t_{heat}) is equal to t_{emit}. Therefore, we can substitute t_{emit} into the definition of Rayleigh number $Ra = t_{heat}\, Ra_f/\tau_0\, Pr$ (see the last paragraph in § 2.1) to quantify the total buoyancy supplied to the fluid at this moment. Specifically, we can substitute $Ra_f/Pr = Ra\, \tau_0/t_{emit}$ into the scaling relation $t_{emit}/\tau_0 \sim Ra_f^{-0.41}\, Pr^{0.41}$, which leads immediately to $t_{emit}/\tau_0 \sim Ra^{-0.69}$. This result is in good agreement with a phenomenological model developed by Howard (1966), who predicted that the onset time for the instability of the TBL scales with Ra as $Ra^{-2/3}$. Similar scaling exponents have been reported in some previous experiments (Vest & Lawson 1972; Davaille & Vatteville 2005). However, these studies determined the onset time by watching the convection patterns instead of measuring the TBL directly, so the correlation between the plume emission and the TBL instability has not been revealed explicitly as in the present study.

Compared to $t_{recover}$ and t_{emit}, the data group t_{static} is relatively scattered and does not collapse well for different Pr. Nevertheless, a simple power-law fit to this data group yields a relation $t_{static}/\tau_0 \sim Ra_f^{-0.38}\, Pr^{0.38}$. If a least squares method is used to determine the best Ra_f and Pr scaling exponents, then we obtain $t_{static}/\tau_0 \sim Ra_f^{-0.49}\, Pr^{0.33}$ (not shown here). The latter scaling relation might be more reasonable, but we do not have a theory for it at this stage. According to figure 4(*b*), t_{static} is the moment when the TBL changes from the recover stage to the quasi-static stage. Thus it is more meaningful to check the time duration for the TBL to recover, i.e. $t_{static} - t_{recover}$. However, no clear Ra_f–Pr dependence is found for this time duration either, so we do not present the data here. It is

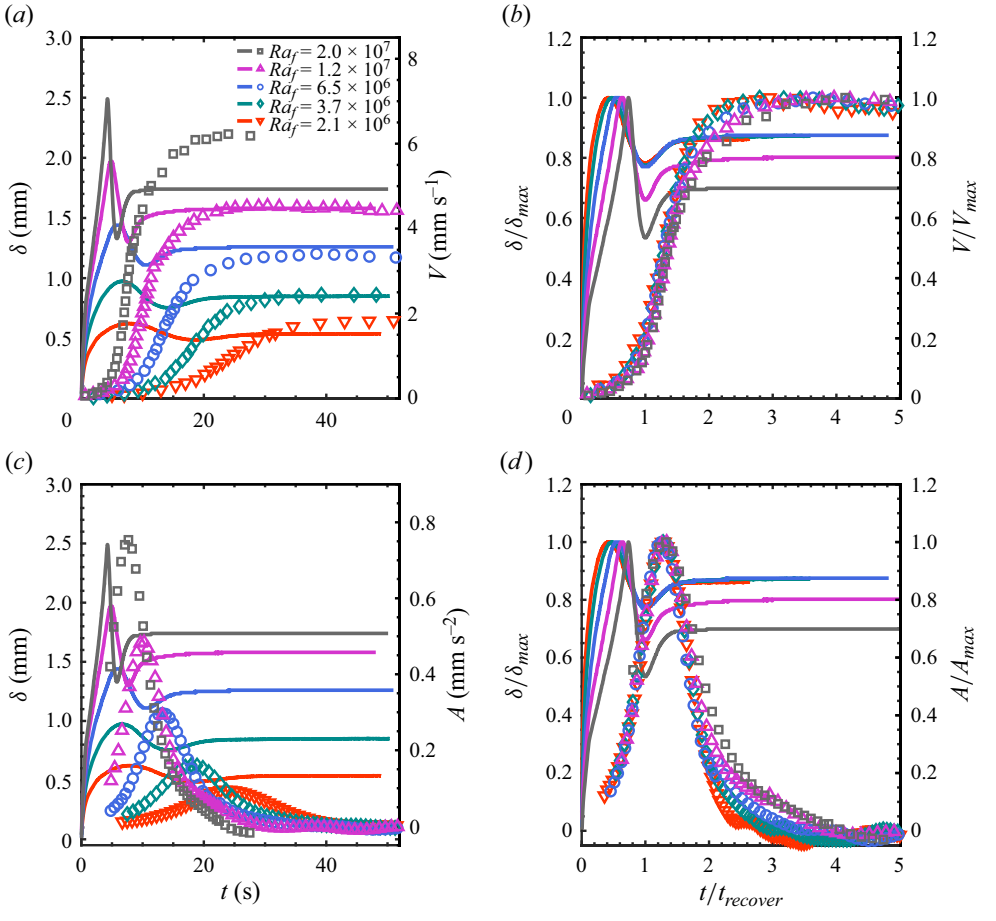

Figure 6. (*a*) Temporal evolution of the TBL thickness determined from shadowgraph (lines) and the plume's rising velocity obtained from PIV (symbols) for different Ra_f at $Pr = 904.7$. (*b*) The same data as in (*a*), but normalized by using the maximum TBL thickness, the maximum rising velocity and $t_{recover}$. Note that these quantities used for normalization have different values for different Ra_f. (*c*,*d*) The relation between the TBL thickness and the plume's acceleration is examined in a similar way as in (*a*,*b*).

noteworthy that a similar recover process exists in turbulent convection experiments due to the so-called finite conductivity effect, which could influence the plume emission and even the heat transport properties (Brown *et al.* 2005; Sun & Xia 2007). It would be interesting to quantify this process in turbulent convection experiments and compare with the present results in future studies.

To further examine the correlation between the plume formation and the TBL development, we plot in figure 6 the plume's rising velocity and the corresponding acceleration together with the TBL thickness. Because similar behaviours have been observed for different Pr, the data measured at $Pr = 904.7$ are taken as the example for discussion. Note that the acceleration plotted here is calculated by taking the time derivative of the rising velocity. A Gaussian convolution method was adopted to reduce the data noise (Mordant *et al.* 2004), so there are no acceleration data at the very beginning of the time series. In addition, the plume has not formed before $t = t_{emit}$, so the velocity and acceleration before this moment are the data inside the TBL. It is seen in figure 6(*a*)

that there is a time delay in the evolution curves between the plume and the TBL. Such a time delay is much clearer in figure 6(*b*), which seems to be a constant in units of $t_{recover}$. While the TBL thickness becomes unchanged after $t \simeq 1.5t_{recover}$, the rising velocity of the plume does not reach the steady state until $t \simeq 2.5t_{recover}$. The time delay can also be observed in the acceleration of the plume (see figures 6*c*,*d*). Noticeably, the normalized accelerations A/A_{max} for different Ra_f almost fall into a single curve once they are plotted against $t/t_{recover}$, just as for the normalized rising velocities V/V_{max} shown in figure 6(*b*). These results not only provide further information about the correlation between the plume formation and the TBL development, but also suggest that $t_{recover}$ is a crucial time scale during the plume evolution process, which will be discussed further in the following subsections.

3.2. *Effects of heating time*

In the previous subsection, we have shown that there exist four distinct stages during the plume formation process. In this subsection, we present a quantitative comparison of the properties of thermal structures emitted at different stages, i.e. generated by different heating times t_{heat}. To examine the effects of t_{heat} in a better way, Ra_f was fixed at $Ra_f = 6.5 \times 10^6$. We first show the results measured at $Pr = 904.7$. The three characteristic times for this Pr at $Ra_f = 6.5 \times 10^6$ are $t_{emit} = 6.6$ s, $t_{recover} = 10.6$ s and $t_{static} = 16.3$ s, so t_{heat} was varied from 3.0 to 16.3 s, corresponding to an Ra ($= t_{heat}\, Ra_f/\tau_0\, Pr$) number range $900 \leq Ra \leq 4900$.

Figure 7(*a*) plots the temporal evolution curves of the rising velocities of thermal structures generated by different t_{heat} (or equivalently different Ra). The data of the starting plume are plotted together for comparison. It is seen that the maximum rising velocities in these curves increase monotonically with increasing t_{heat}, and the upper limit is bounded by the case of the starting plume. Based on their variation trends, these curves can be divided into two groups. For thermal structures generated by $t_{heat} \geq t_{emit}$ ($= 6.6$ s), their rising velocities first increase quickly in a manner like the starting plume, and then decay slowly like a thermal after reaching the maximum value (demonstrated in § 3.3). Note that these thermal structures can be viewed as detached TBLs, so their almost-collapsed curves in the accelerating stage could be originated from the dynamics inherited from the unstable TBL, which is commonly believed in studies of Rayleigh–Bénard convection (Ahlers *et al.* 2009). However, for the cases with $t_{heat} < t_{emit}$, their rising velocities show a different trend in the accelerating stage. This is because these thermal structures are not emitted from the TBL due to instability. Rather, they are hot fluid parcels adjacent to the heat source, which go up after the heating power is turned off thanks to their own buoyancy. In this context, their generation process is similar to a sudden release of a hot fluid parcel in some experimental studies of thermals (see e.g. Griffiths 1986).

The acceleration plotted in figure 7(*b*) confirms that t_{emit} is the characteristic time that determines whether thermal structures generated by finite t_{heat} will have similar evolution dynamics. It is seen clearly that the accelerations of thermal structures with $t_{heat} < t_{emit}$ are much weaker than in the cases with $t_{heat} \geq t_{emit}$, and exhibit an obvious different trend in the accelerating stage. For thermal structures with $t_{heat} \geq t_{emit}$, their acceleration curves largely follow the trend of the starting plume, except for the decay behaviour. To be specific, the acceleration of the starting plume decreases monotonically from the maximum value to a steady level close to zero. By contrast, the data for thermal structures with $t_{heat} \geq t_{emit}$ first decay to negative values that are well below zero, and then increase gradually to the level of the starting plume. A close look at figures 7(*a*,*b*) reveals that

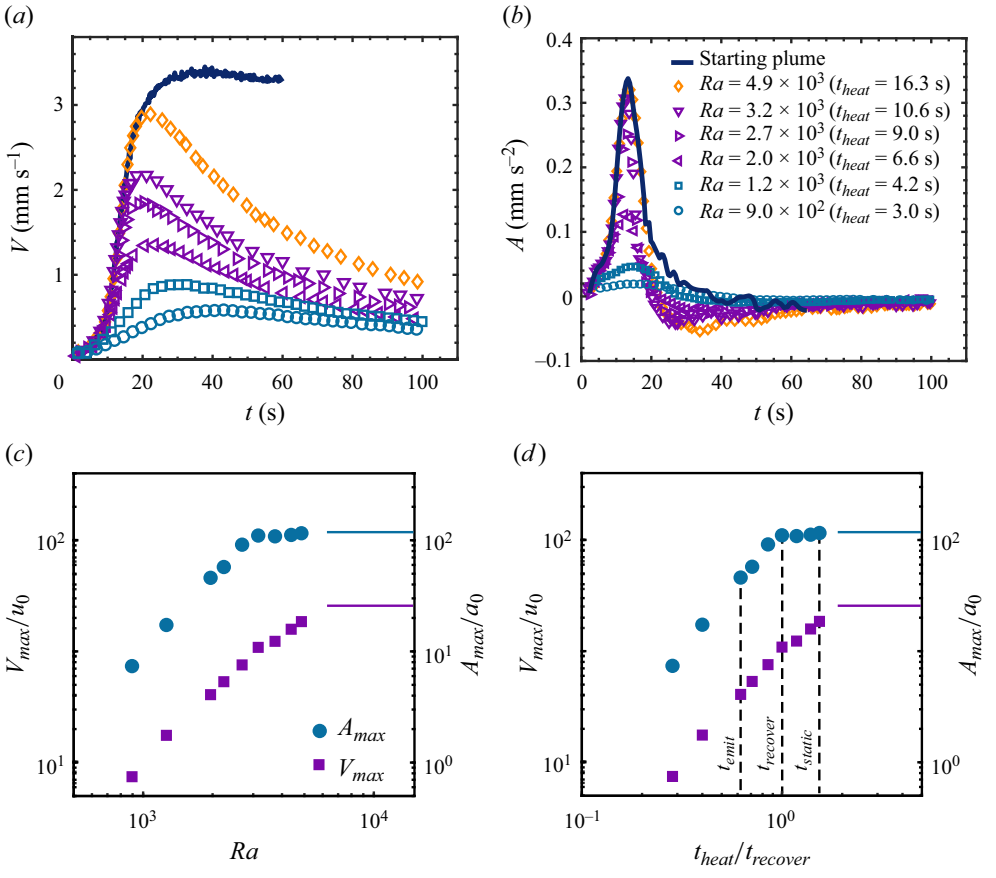

Figure 7. (*a*,*b*) Temporal variations of (*a*) the rising velocity and (*b*) the corresponding acceleration of thermal structures generated by different heating times (or equivalently different Ra) at $Pr = 904.7$ and $Ra_f = 6.5 \times 10^6$. (*c*,*d*) The dimensionless maximum velocity V_{max}/u_0 and the dimensionless maximum acceleration A_{max}/a_0 as functions of (*c*) Ra and (*d*) the dimensionless heating time $t_{heat}/t_{recover}$. The corresponding values of the starting plume are indicated by the purple solid line (dimensionless maximum velocity) and the blue solid line (dimensionless maximum acceleration), respectively.

the moment when the acceleration drops to zero is the moment when the rising velocity reaches the maximum value. This phenomenon can be found for all the thermal structures generated by finite t_{heat}, though it is not that obvious for the cases with $t_{heat} < t_{emit}$. To understand this result, we note that thermal structures generated by finite t_{heat} do not have an energy supply after the heating power is turned off, thus the viscous drag becomes significant in the decelerating stage and leads to negative accelerations. As the viscous drag is larger for larger rising velocity, one can see in figure 7(*b*) that the drop in acceleration is stronger for larger t_{heat}.

To examine quantitatively how t_{heat} affects the properties of thermal structures, we take the maximum velocity and the maximum acceleration as the characteristic quantities, and plot their dimensionless values in figures 7(*c*,*d*). It is seen that the maximum velocity increases with Ra (or the dimensionless heating time $t_{heat}/t_{recover}$) and approaches the value of the starting plume gradually. Based on the variation trend of V_{max}/u_0 in figure 7(*d*), the maximum velocity of thermal structures generated by finite t_{heat} will be equal to the value of the starting plume when $t_{heat} \simeq 2.5 t_{recover}$. This time scale is

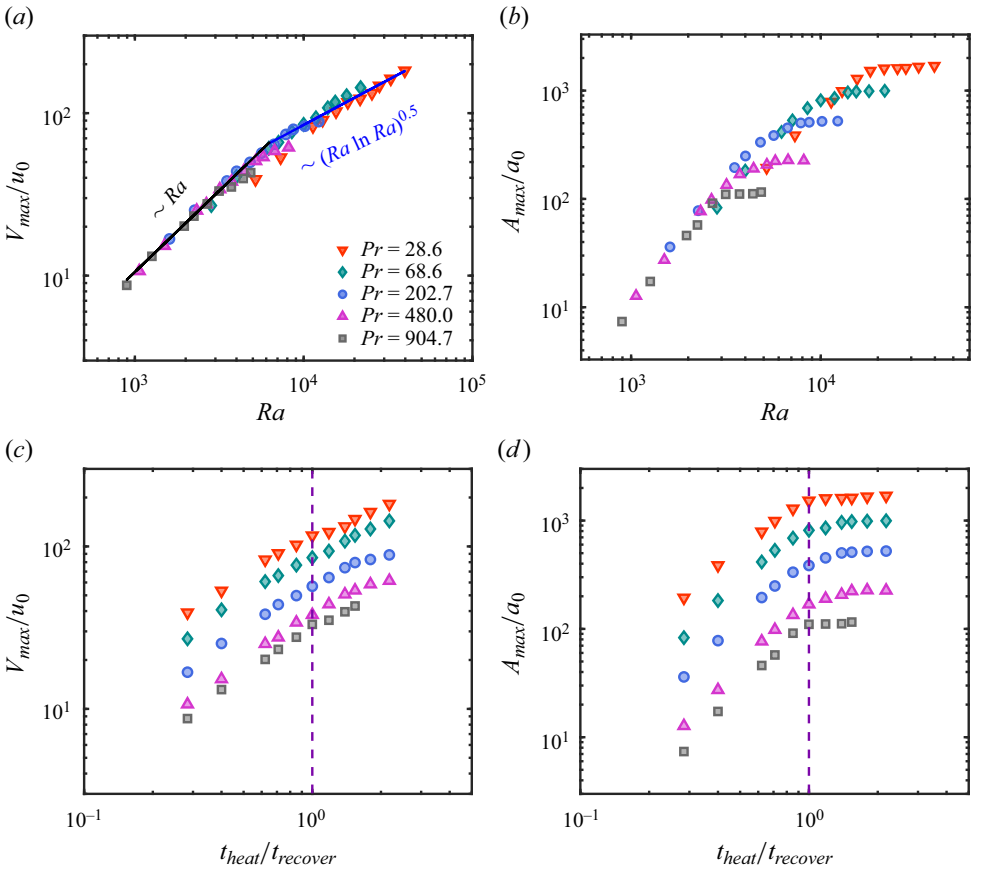

Figure 8. (*a*,*c*) The dimensionless maximum velocity V_{max}/u_0 and (*b*,*d*) the dimensionless maximum acceleration A_{max}/a_0 as functions of (*a*,*b*) Ra, and (*c*,*d*) the dimensionless heating time $t_{heat}/t_{recover}$ for different Pr at $Ra_f = 6.5 \times 10^6$. The black and blue solid lines in (*a*) are two different power laws, as labelled.

consistent with the data shown in figure 6(*b*), where one can see that the rising velocity of the thermal structure reaches the steady state at approximately $2.5t_{recover}$.

The maximum acceleration A_{max}/a_0 also increases with $t_{heat}/t_{recover}$ and reaches the value of the starting plume at $t_{heat} \simeq t_{recover}$. For larger t_{heat}, A_{max}/a_0 remains unchanged. This behaviour could be understood as follow. Although the thermal structure begins to emit at t_{emit}, the emission process does not complete until $t_{recover}$. During the emission process, the thermal structure can gain buoyancy energy from the TBL directly, so its acceleration can increase to a larger value if the heating power supply is continued. At the moment of $t_{recover}$, the thermal structure is fully detached from the TBL, and its buoyancy energy is fed by the long tail after then, just as in the case of the starting plume. Therefore, the maximum acceleration reaches the value of the starting plume at $t_{heat} = t_{recover}$. And because the rising velocity does not reach the maximum value until the acceleration becomes zero, the maximum velocity approaches the value of the starting plume at a larger value of $t_{heat}/t_{recover}$.

These asymptotic behaviours can be observed for all the Pr explored in the present study. As shown in figures 8(*c*,*d*), while V_{max}/u_0 for different Pr seem to approach the upper limit values at different $t_{heat}/t_{recover}$, A_{max}/a_0 for different Pr reach different plateaus roughly at

the same condition ($t_{heat}/t_{recover} \simeq 1$). Noticeably, if A_{max}/a_0 is plotted against Ra, then the values almost fall onto a single curve before reaching the plateaus (see figure 8*b*). A more remarkable finding comes from the data shown in figure 8(*a*). It is seen that V_{max}/u_0 for different Pr collapse well over the present Ra number range. However, these data do not follow a simple scaling law. Instead, they experience a transition from $V_{max}/u_0 \sim Ra$ to $V_{max}/u_0 \sim (Ra \ln Ra)^{0.5}$ at $Ra \simeq 6000$. To understand this scaling transition, we note that thermal structures generated by finite t_{heat} contain finite amounts of buoyancy and thus can be viewed as thermals. However, according to the data shown in figure 6(*b*), if t_{heat} is larger than $2.5t_{recover}$, then these thermal structures will get into the quasi-static stage and go up with constant rising velocities like plumes. Since the maximum heating times examined in figure 8 are all smaller than $2.5t_{recover}$, these data can be understood by the behaviours of thermals. For the scaling relation below $Ra \simeq 6000$, it is consistent with previous studies of thermals at low Ra (Morton 1960; Shlien & Thompson 1975); for that above $Ra \simeq 6000$, it is in excellent agreement with the model prediction and the numerical results by Whittaker & Lister (2008). Interestingly, if a simple power law is attempted to fit all the data in figure 8(*a*), then the scaling relation turns out to be $V_{max}/u_0 \sim Ra^{0.78}$ (not shown in the figure for clarity), which is in line with the experimental finding and the model prediction ($V_{max}/u_0 \sim Ra^{0.75}$) by Griffiths (1986). Therefore, the present data provide not only experimental evidence for the existence of the $(Ra \ln Ra)^{0.5}$ scaling for thermals at large Ra, but also a unifying understanding of the seemingly inconsistent scaling relations observed in previous studies (Morton 1960; Shlien & Thompson 1975; Griffiths 1986; Whittaker & Lister 2008).

3.3. *Characteristics of thermal structures generated by $t_{heat} = t_{recover}$*

Based on the results presented in §§ 3.1 and 3.2, we have found that $t_{recover}$ is a crucial time scale during the formation and evolution of thermal structures. In particular, it is the critical moment when the thermal structure is fully detached from the TBL and the corresponding maximum acceleration reaches an upper limit. Since thermal structures generated by different heating times t_{heat} have similar evolution dynamics once $t_{heat} \geq t_{emit}$, we can take the case with $t_{heat} = t_{recover}$ as an example to examine their evolution dynamics in detail, which is the focus of this subsection. Again, we will present first the results measured at $Pr = 904.7$ and then the data for different Pr.

Figure 9 shows the evolution curves of the rising velocities of thermal structures generated by $t_{heat} = t_{recover}$ for different Ra_f at $Pr = 904.7$. The data have been plotted in different ways to show every detailed feature during the evolution. It is seen in figure 9(*a*) that the curves for different Ra_f have a similar shape, where the higher Ra_f case has a larger maximum rising velocity V_{max} that occurs at a shorter time. If we take V_{max} and $t_{recover}$ as the referenced units, then the normalized velocity V/V_{max} as a function of $t/t_{recover}$ for different Ra_f collapses onto a universal curve when $t/t_{recover} \leq 2.5$ (see figure 9*b*). The three characteristic times for the $Ra_f = 6.5 \times 10^6$ case are also highlighted in figure 9(*b*), indicating that the evolution trends are different before and after t_{emit}. However, we note that the data collapse could not be achieved by using t_{emit} as the referenced time. Moreover, the universal behaviour applies only to the data within $t/t_{recover} \simeq 2.5$, after which the data for different Ra_f become diverged (see the inset of figure 9*b*).

For the time period $t/t_{recover} > 2.5$, the thermal structures have got into the decelerating stage without heat supply and are dominant by the viscous drag. Therefore, we take the diffusion velocity u_0 ($= r_0/\tau_0$) as the referenced velocity, and plot V/u_0 as a function of $t/t_{recover}$ in figure 9(*c*). Although this dimensionless form does not yield a data collapse,

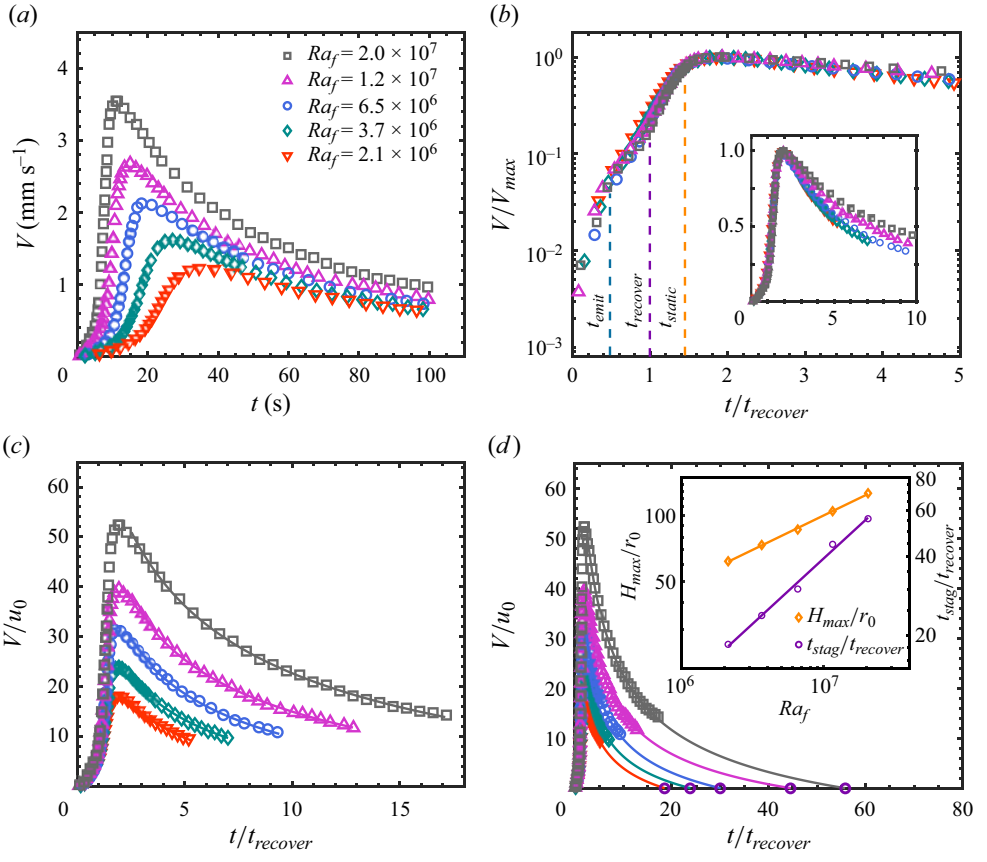

Figure 9. (*a*) Temporal variations of the rising velocities of thermal structures generated by $t_{heat} = t_{recover}$ for different Ra_f at $Pr = 904.7$. (*b*) The same results as in (*a*), but normalized by the maximum rising velocity V_{max} and the characteristic time $t_{recover}$ for each Ra_f. The inset shows that the data for different Ra_f begin to diverge when $t/t_{recover} \gtrsim 2.5$. (*c*) A similar plot as in (*b*), but the data are normalized by the diffusive velocity u_0 ($= r_0/\tau_0$). The solid curves are the best fits to each data set for $t/t_{recover} \gtrsim 2.5$. (*d*) The same data as in (*c*), with the fitting curves extended to the stagnant time t_{stag}, at which the rising velocity becomes zero and the thermal structure reaches the maximum ascent height H_{max}. Inset: the dimensionless stagnant time $t_{stag}/t_{recover}$ and the dimensionless maximum ascent height H_{max}/r_0 as functions of Ra_f. The solid lines are power-law fits to each data set: $t_{stag}/t_{recover} \sim Ra_f^{0.50}$ and $H_{max}/r_0 \sim Ra_f^{0.31}$. See text for detailed explanations.

the data in the decelerating stage ($t/t_{recover} > 2.5$) for different Ra_f exhibit a similar shape and can be fitted by a relation $V/u_0 \sim (t/t_{recover} - 1)^{-0.5} - V_{virt}$, which is proposed to describe the evolution behaviour of thermals (Morton 1960; Griffiths 1986). Here, V_{virt} is known as the virtual velocity, as the rising velocity should approach zero as the time goes to infinity.

Actually, thermal structure generated by a finite heating time should have a finite lifetime. With this in mind, we define the stagnant time t_{stag} when the rising velocity decays to zero. At this moment, the thermal structure becomes stagnant and reaches the maximum ascent height H_{max}. Figure 9(*d*) illustrates how this characteristic time is determined from the decay curves of the rising velocity. The dimensionless stagnant time $t_{stag}/t_{recover}$ thus determined is found to scale with Ra_f as $t_{stag}/t_{recover} \sim Ra_f^{0.50}$ (see the inset of figure 9*d*). As $t_{recover}/\tau_0 \sim Ra_f^{-0.48}$, we can infer that t_{stag} is almost independent of Ra_f, implying that

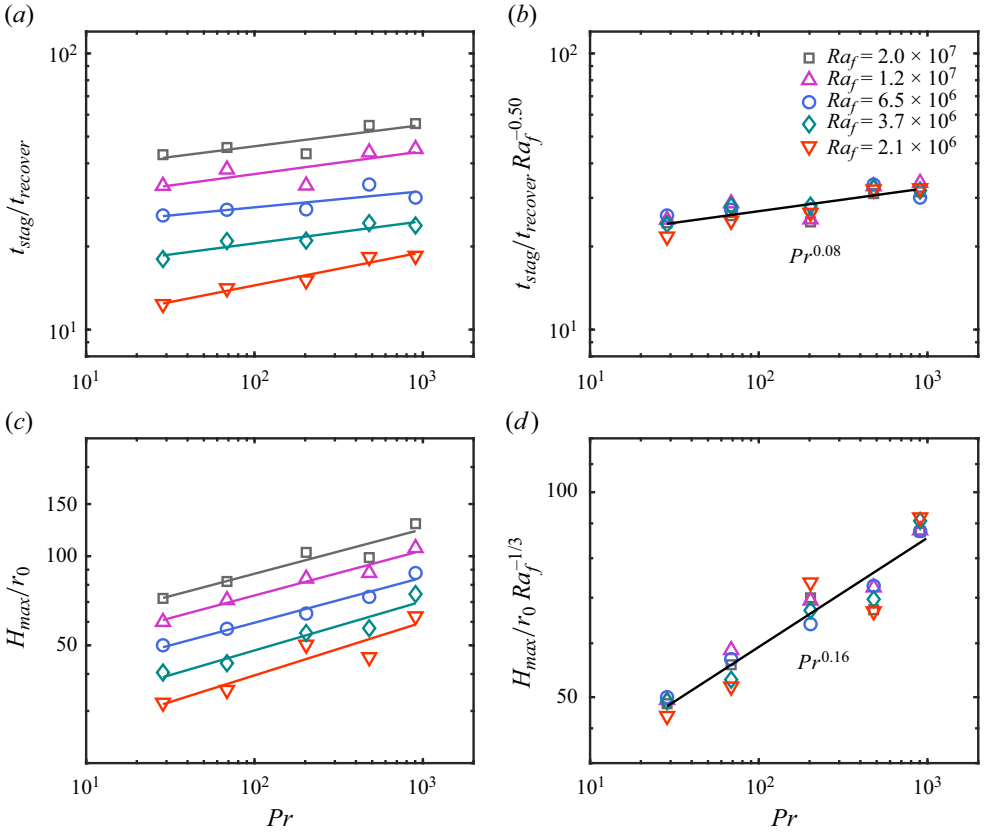

Figure 10. (*a*) The dimensionless stagnant time $t_{stag}/t_{recover}$ as a function of Pr for different Ra_f. The solid lines are power-law fits to each data set. (*b*) Plots of $t_{stag}/t_{recover}$ compensated by $Ra_f^{0.50}$ as a function of Pr. The solid line is the best power-law fit to all the data points: $t_{stag}/t_{recover} \sim Ra_f^{0.50}\,Pr^{0.08}$. (*c*) The dimensionless maximum ascent height H_{max}/r_0 as a function of Pr for different Ra_f. The solid lines are power-law fits to each data set. (*d*) Plots of H_{max}/r_0 compensated by $Ra_f^{1/3}$ as a function of Pr. The solid line is the best power-law fit to all the data points: $H_{max}/r_0 \sim Ra_f^{1/3}\,Pr^{0.16}$.

this time scale is determined by a diffusion process. The corresponding maximum ascent height H_{max} can also be obtained by integrating the rising velocity to the moment $t = t_{stag}$. The data thus obtained are plotted in the inset of figure 9(*d*), and they follow a scaling relation as $H_{max}/r_0 \sim Ra_f^{0.31}$. This scaling exponent coincides with the predicted scaling $1/3$ by a theoretical model of turbulent atmospheric plumes (Stothers 1989), despite the present scenario being laminar thermal structures in a homogeneous stationary fluid layer.

The analysis above suggests three characteristic quantities for further examination with different Pr: the maximum rising velocity V_{max} during the evolution, the stagnant time t_{stag}, and the maximum ascent height H_{max}. We first check the Pr dependencies of t_{stag} and H_{max}. Figure 10(*a*) shows the dimensionless stagnant time $t_{stag}/t_{recover}$ as a function of Pr for different Ra_f. It is seen that these data sets can all be described by power-law fittings, with the scaling exponents ranging from 0.06 to 0.12. Because the Ra_f-dependent scalings of $t_{stag}/t_{recover}$ are close to 0.50 for all Pr (not shown here), we compensate the data in figure 10(*a*) by $Ra_f^{0.50}$ to collapse them into a single line (see figure 10*b*); then a power-law fit to all the data yields a Pr-dependent scaling 0.08, i.e. $t_{stag}/t_{recover} \sim Ra_f^{0.50}\,Pr^{0.08}$, or

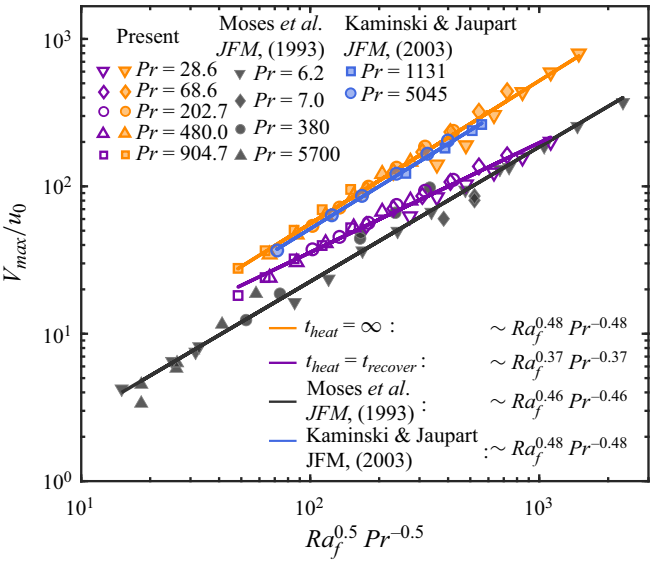

Figure 11. The dimensionless maximum rising velocities of thermal structures as functions of $Ra_f^{0.5}\, Pr^{-0.5}$ for different parameter settings. The results obtained in previous studies by Moses *et al.* (1993) and Kaminski & Jaupart (2003) are plotted for comparison. See text for a detailed explanation.

equivalently, $t_{stag}/\tau_0 \sim Ra_f{}^{0.02}\, Pr^{0.56}$. Through a similar procedure, we obtain the Ra_f–Pr dependence of the maximum ascent height as $H_{max}/r_0 \sim Ra_f{}^{1/3}\, Pr^{0.16}$ (see figures 10*c*,*d*). To the best of our knowledge, no theory has studied the stagnant time before. However, the maximum ascent height has received much of interest, as it is relevant to a range of natural phenomena, such as cloud rise and volcanic eruption (Wilson *et al.* 1978; Sparks 1986; Stothers 1989; Hansen *et al.* 2006; Glaze *et al.* 2017). The scaling relations obtained here, especially the less-explored Pr dependencies, might be helpful to understand the relevant processes in nature.

Finally, we examine the maximum rising velocity V_{max} of thermal structures generated by $t_{heat} = t_{recover}$ in figure 11. Also plotted in the figure are the results of starting plumes obtained in two previous studies (Moses *et al.* 1993; Kaminski & Jaupart 2003) as well as in the present work. Note that for starting plumes, their maximum rising velocities are the values at the steady state (see figure 6*b*). According to Moses *et al.* (1993), the dimensionless maximum rising velocities of starting plumes V_{max}/u_0 obey a scaling law as $V_{max}/u_0 \sim Ra_f^{0.5}\, Pr^{-0.5}$. This scaling law is supported by their experimental data obtained by the shadowgraph technique, which can be described by a relation $Ra_f^{0.46}\, Pr^{-0.46}$ approximately. However, by conducting new measurements with the differential interferometry technique, Kaminski & Jaupart (2003) found that starting plumes can rise much faster than the results reported by Moses *et al.* (1993), though the scaling exponents in these two studies are basically consistent (see black and blue lines in figure 11). As discussed by Kaminski & Jaupart (2003), the discrepancy in magnitude could be due to some experimental artefacts, such as sidewall effects, free-surface effects and thermal leakage. Our present results obtained by PIV measurements over a different Pr range are in good agreement with the data by Kaminski & Jaupart (2003), including both the scaling exponent and the magnitude. This good agreement provides support for the study by Kaminski & Jaupart (2003) on the one hand, and verifies the reliability of the present experiments on the other.

In contrast to the behaviour of starting plumes, V_{max}/u_0 of thermal structures generated by $t_{heat} = t_{recover}$ exhibit a different Ra_f–Pr dependence. A simple power-law fit to these data yields a scaling relation $V_{max}/u_0 \sim Ra_f^{0.37}\, Pr^{-0.37}$. If a least squares method is used to fit this data group, then the Ra_f and Pr scaling exponents change little, being 0.41 and -0.37, respectively (not shown here). To understand this scaling relation, we define a Reynolds number Re as $Re = V_{max} r_0/\nu$ based on this data group. By using the definitions of τ_0, u_0, Ra and Pr, namely $\tau_0 = r_0^2/\kappa$, $u_0 = r_0/\tau_0 = r_0\, Pr/\nu$ and $Ra = t_{heat}\, Ra_f/\tau_0\, Pr$, and noticing that $t_{heat} = t_{recover}$ for this data group where $t_{recover}/\tau_0 \sim Ra_f^{-0.48}\, Pr^{0.48}$, we obtain $Re \sim Ra^{0.71}\, Pr^{-1}$. This result recalls the scaling relation $Re \sim Ra^{2/3}\, Pr^{-1}$ predicted by a theoretical model for large-Pr natural thermal convection (Shishkina *et al.* 2017). It is also worth mentioning that in previous studies of turbulent Rayleigh–Bénard convection with large Pr (Lam *et al.* 2002; Silano, Sreenivasan & Verzicco 2010; Li *et al.* 2021*a*), the observed Re–Ra scaling exponents (ranging from 0.65 to 0.74) are compatible with the present value. However, it should be stressed that the convection systems examined in these studies (Lam *et al.* 2002; Silano *et al.* 2010; Shishkina *et al.* 2017; Li *et al.* 2021*a*) are turbulent flows, while the present study addresses laminar thermal structures. Thus it is interesting to see the good match of the scaling exponents between different studies. One possible explanation is that large-Pr thermal convection is dominant by slender thermal structures, and no large-scale mean flow exists in the system (Li *et al.* 2021*a*). As a result, the flow velocity first increases with growing distance away from the boundary, and then decays slowly to zero after reaching the maximum, which is similar to the present situation. These similar flow features might be the origin of the similar scaling relations observed in different studies.

4. Conclusion

In summary, we have conducted a series of experiments to investigate the formation and evolution of laminar thermal structures generated by a small heat source. The experiments were performed over the flux Rayleigh number Ra_f range $2.1 \times 10^6 \leq Ra_f \leq 3.6 \times 10^7$ and the Prandtl number Pr range of $28.6 \leq Pr \leq 904.7$. In order to examine the properties of thermal structures generated by finite heating time t_{heat}, t_{heat} was also varied in some experiments, with Ra_f fixed at 6.5×10^6, resulting in a Rayleigh number Ra range $900 \leq Ra \leq 4 \times 10^4$. Based on the experimental data with different parameter settings ($\sim$110 cases in total), we came to the main findings below.

First, through examining the correlation between the plume formation and the thermal boundary layer (TBL) development, three characteristic times were observed during the plume formation process, namely t_{emit}, $t_{recover}$ and t_{static}. Specifically, when the plume starts to emit due to the TBL instability, the TBL thickness reaches a maximum that gives rise to the determination of t_{emit}. As the plume emits, the TBL thickness decreases and reaches a local minimum when the plume's head is completely detached from the TBL. This critical moment $t_{recover}$ turns out to be the build-up time for starting plumes as evaluated (without direct measurements) in the literature (Moses *et al.* 1993). The Ra_f–Pr dependencies of t_{emit} and $t_{recover}$ are found to be $Ra_f^{-0.41}\, Pr^{0.41}$ and $Ra_f^{-0.48}\, Pr^{0.48}$, respectively, which are in good agreement with the theories (Howard 1966; Moses *et al.* 1993). As for t_{static}, it is the moment when the TBL gets into the steady state and obeys a scaling relation $Ra_f^{-0.49}\, Pr^{0.33}$. The plume reaches the steady state with a time delay, which is a constant in units of $t_{recover}$.

Based on these characteristic times, the effects of heating time t_{heat} on thermal structures were investigated. It is found that once $t_{heat} \gtrsim t_{emit}$, thermal structures generated by different t_{heat} will have similar evolution dynamics, with the accelerating stage like starting plumes, and the decay stage like thermals. In particular, by using the diffusion velocity as the normalized unit, the dimensionless maximum rising velocities of these thermal structures exhibit a universal behaviour, which experiences a crossover in the scaling relation from Ra to $(Ra \ln Ra)^{0.5}$ as Ra increases (by increasing t_{heat}). This finding not only provides experimental evidence for the theoretically predicted scaling $(Ra \ln Ra)^{0.5}$ for thermals at large-Ra (Whittaker & Lister 2008), but also explains the inconsistent results reported in previous studies of thermals (Morton 1960; Shlien & Thompson 1975; Griffiths 1986; Whittaker & Lister 2008; Peng & Lister 2014).

It is further found that the maximum accelerations of thermal structures generated by finite t_{heat} have a saturated value bounded by the case of starting plumes. This saturation occurs at $t_{heat} \simeq t_{recover}$, implying that $t_{recover}$ is a crucial time scale during the evolution process of these thermal structures. Therefore, the characteristics of thermal structures generated by $t_{heat} = t_{recover}$ were examined in detail. The most interesting findings about these thermal structures are their maximum ascent height H_{max} and maximum rising velocity V_{max}, which follow the scaling relations $Ra_f^{1/3}\, Pr^{0.16}$ and $Ra_f^{0.37}\, Pr^{-0.37}$, respectively. It is not clear at this stage how t_{heat} would affect these two scaling relations. Further investigations should be conducted to address this issue quantitatively.

Before ending this paper, we would like to highlight one issue that is relevant to one of the motivations of the present study. As we discussed in the Introduction, the emission of thermal structures in turbulent Rayleigh–Bénard convection is a co-action of the TBL instability and the perturbation from turbulent flow. As a result, the thermal structures emit at different stages from the TBL and thus supply different amounts of buoyancy energy to drive the convection flow. It is not clear whether these thermal structures would exhibit different behaviours and contribute to the anomalous scaling observed in turbulent Rayleigh–Bénard convection (Brown, Funfschilling & Ahlers 2007; Ching 2007; Li *et al.* 2021*b*). In the present study, we have shown that once thermal structures emit at a time scale larger than the onset time that determines the TBL instability, they will have similar evolution dynamics, despite the magnitudes of their rising velocity and acceleration being different. However, this result was obtained in a stationary fluid layer without a background flow. It would be interesting to check the present finding by imposing a mean flow above the heat source, which is beyond the scope of the present study but an exciting issue to explore in the future.

Supplementary movie. A supplementary movie is available at https://doi.org/10.1017/jfm.2024.266.

Acknowledgements. We thank L. Sun for participating in the early stage of this project.

Funding. This work was supported by the National Natural Science Foundation of China (NSFC grant nos 12272162, 11961160719 and 11702128) and the Department of Science and Technology of Guangdong Province (grant no. 2023B1212060001). P.W. was supported in part by an NSFC grant (no. 11872281).

Declaration of interests. The authors report no conflict of interest.

Author ORCIDs.
Ping Wei https://orcid.org/0000-0002-2268-9086;
Shi-Di Huang https://orcid.org/0000-0001-5719-6428.

References

AHLERS, G., GROSSMANN, S. & LOHSE, D. 2009 Heat transfer and large scale dynamics in turbulent Rayleigh–Bénard convection. *Rev. Mod. Phys.* **81**, 503–537.

BATCHELOR, G.K. 1954 Heat convection and buoyancy effects in fluids. *Q. J. R. Meteorol. Soc.* **80**, 339–358.

BHAGANAGAR, K. & BHIMIREDDY, S.R. 2020 Numerical investigation of starting turbulent buoyant plumes released in neutral atmosphere. *J. Fluid Mech.* **900**, A32.

BHAMIDIPATI, N. & WOODS, A.W. 2017 On the dynamics of starting plumes. *J. Fluid Mech.* **833**, R2.

BOND, D. & JOHARI, H. 2005 Effects of initial geometry on the development of thermals. *Exp. Fluids* **39**, 591–601.

BROWN, E., FUNFSCHILLING, D. & AHLERS, G. 2007 Anomalous Reynolds-number scaling in turbulent Rayleigh–Bénard convection. *J. Stat. Mech.* **2007**, P10005.

BROWN, E., NIKOLAENKO, A., FUNFSCHILLING, D. & AHLERS, G. 2005 Heat transport in turbulent Rayleigh–Bénard convection: effect of finite top- and bottom-plate conductivities. *Phys. Fluids* **17**, 075108.

CHING, E.S. 2007 Scaling laws in the central region of confined turbulent thermal convection. *Phys. Rev.* E **75**, 056302.

DAVAILLE, A., LIMARE, A., TOUITOU, F., KUMAGAI, I. & VATTEVILLE, J. 2011 Anatomy of a laminar starting thermal plume at high Prandtl number. *Exp. Fluids* **50**, 285–300.

DAVAILLE, A. & VATTEVILLE, J. 2005 On the transient nature of mantle plumes. *Geophys. Res. Lett.* **32**, L14309.

FUJII, T. 1963 Theory of the steady laminar natural convectiol above a horizontal line heat source and a point heat source. *Intl J. Heat Mass Transfer* **6**, 597–606.

FUJII, T., MORIOKA, I. & UEHARA, H. 1973 Buoyant plume above a horizontal line heat source. *Intl J. Heat Mass Transfer* **16**, 755–768.

FUNFSCHILLING, D. & AHLERS, G. 2004 Plume motion and large-scale circulation in a cylindrical Rayleigh–Bénard cell. *Phys. Rev. Lett.* **92**, 194502.

GEBHART, B., PERA, L. & SCHORR, A.W. 1970 Steady laminar natural convection plumes above a horizontal line heat source. *Intl J. Heat Mass Transfer* **13**, 161–171.

GLAZE, L.S., SELF, S., SCHMIDT, A. & HUNTER, S.J. 2017 Assessing eruption column height in ancient flood basalt eruptions. *Earth Planet. Sci. Lett.* **457**, 263–270.

GRIFFITHS, R.W. 1986 Thermals in extremely viscous fluids, including the effects of temperature-dependent viscosity. *J. Fluid Mech.* **166**, 115–138.

HANSEN, C.J., ESPOSITO, L., STEWART, A.I.F., COLWELL, J., HENDRIX, A., PRYOR, W. & WEST, R. 2006 Enceladus' water vapor plume. *Science* **311**, 1422–1425.

HAY, W.A. & PAPALEXANDRIS, M.V. 2020 Evaporation-driven turbulent convection in water pools. *J. Fluid Mech.* **904**, A14.

HELFRICH, K.R. 1994 Thermals with background rotation and stratification. *J. Fluid Mech.* **259**, 265–280.

HOWARD, L.N. 1966 Convection at high Rayleigh number. In *Applied Mechanics* (ed. H. Görtler), pp. 1109–1115. Springer.

JELLINEK, A.M. & MANGA, M. 2004 Links between long-lived hot spots, mantle plumes, D'', and plate tectonics. *Rev. Geophys.* **42**, RG3002.

JIANG, Y., NIE, B. & XU, F. 2019*a* Lapping flow and starting plume on an evenly heated horizontal plate. *Intl J. Heat Mass Transfer* **138**, 235–243.

JIANG, Y., NIE, B. & XU, F. 2019*b* Scaling laws of buoyant flows on a suddenly heated horizontal plate. *Intl Commun. Heat Mass Transfer* **105**, 58–64.

JIANG, Y., NIE, B., ZHAO, Y., CARMELIET, J. & XU, F. 2021 Scaling of buoyancy-driven flows on a horizontal plate subject to a ramp heating of a finite time. *Intl J. Heat Mass Transfer* **171**, 121061.

KADANOFF, L.P. 2001 Turbulent heat flow: structures and scaling. *Phys. Today* **54**, 34–39.

KAMINSKI, E. & JAUPART, C. 2003 Laminar starting plumes in high-Prandtl-number fluids. *J. Fluid Mech.* **478**, 287–298.

VAN KEKEN, P.E., DAVAILLE, A. & VATTEVILLE, J. 2013 Dynamics of a laminar plume in a cavity: the influence of boundaries on the steady state stem structure. *Geochem. Geophys. Geosyst.* **14**, 158–178.

KONDRASHOV, A., SBOEV, I. & DUNAEV, P. 2016*a* Evolution of convective plumes adjacent to localized heat sources of various shapes. *Intl J. Heat Mass Transfer* **103**, 298–304.

KONDRASHOV, A., SBOEV, I. & RYBKIN, K. 2016*b* Effect of boundary conditions on thermal plume growth. *Heat Mass Transfer* **52**, 1359–1368.

LAM, S., SHANG, X.D., ZHOU, S.Q. & XIA, K.-Q. 2002 Prandtl number dependence of the viscous boundary layer and the Reynolds numbers in Rayleigh–Bénard convection. *Phys. Rev.* E **65**, 066306.

LI, X.-M., HE, J.D., TIAN, Y., HAO, P. & HUANG, S.-D. 2021*a* Effects of Prandtl number in quasi-two-dimensional Rayleigh–Bénard convection. *J. Fluid Mech.* **915**, A60.

LI, X.-M., HUANG, S.-D., NI, R. & XIA, K.-Q. 2021*b* Lagrangian velocity and acceleration measurements in plume-rich regions of turbulent Rayleigh–Bénard convection. *Phys. Rev. Fluids* **6**, 053503.
LITHGOW-BERTELLONI, C., RICHARDS, M.A., CONRAD, C.P. & GRIFFITHS, R.W. 2001 Plume generation in natural thermal convection at high Rayleigh and Prandtl numbers. *J. Fluid Mech.* **434**, 1–21.
MALKUS, W.V.R. 1954 The heat transport and spectrum of thermal turbulence. *Proc. R. Soc. Lond.* A **225**, 196–212.
MARAGATHAM, G. & ROOMI, S.M. 2015 A review of image contrast enhancement methods and techniques. *Res. J. Appl. Sci.* **5**, 309–326.
MORDANT, N., CRAWFORD, A.M. & BODENSCHATZ, E. 2004 Experimental Lagrangian acceleration probability density function measurement. *Physica* D **193**, 245–251.
MORTON, B.R. 1960 Weak thermal vortex rings. *J. Fluid Mech.* **9**, 107–118.
MORTON, B.R., TAYLOR, G.I. & TURNER, J.S. 1956 Turbulent gravitational convection from maintained and instantaneous sources. *Proc. R. Soc. Lond.* A **234**, 1–23.
MOSES, E., ZOCCHI, G. & LIBCHABERII, A. 1993 An experimental study of laminar plumes. *J. Fluid Mech.* **251**, 581–601.
MOSES, E., ZOCCHI, G., PROCACCIA, I. & LIBCHABER, A. 1991 The dynamics and interaction of laminar thermal plumes. *Europhys. Lett.* **14**, 55–60.
ORLANDI, P. & CARNEVALE, G.F. 2020 Numerical simulations of thermals with and without stratification. *J. Fluid Mech.* **899**, A37.
PENG, G.G. & LISTER, J.R. 2014 The initial transient and approach to self-similarity of a very viscous buoyant thermal. *J. Fluid Mech.* **744**, 352–375.
PERA, L. & GEBHART, B. 1971 On the stability of laminar plumes: some numerical solutions and experiments. *Intl J. Heat Mass Transfer* **14**, 975–984.
RAFFEL, M., WILLERT, C.E., SCARANO, F., KÄHLER, C.J., WERELEY, S.T. & KOMPENHANS, J. 2018 *Particle Image Velocimetry: A Practical Guide*. Springer.
SETTLES, G.S. 2001 *Schlieren and Shadowgraph Techniques*. Springer.
SHISHKINA, O., EMRAN, M.S., GROSSMANN, S. & LOHSE, D. 2017 Scaling relations in large-Prandtl-number natural thermal convection. *Phys. Rev. Fluids* **2**, 103502.
SHISHKINA, O., HORN, S., WAGNER, S. & CHING, E.S.C. 2015 Thermal boundary layer equation for turbulent Rayleigh–Bénard convection. *Phys. Rev. Lett.* **114**, 114302.
SHLIEN, D.J. 1976 Some laminar thermal and plume experiments. *Phys. Fluids* **19**, 1089–1098.
SHLIEN, D.J. 1979 Relations between point sources buoyant convection phenomena. *Phys. Fluids* **22**, 2277–2283.
SHLIEN, D.J. & BOXMAN, R.L. 1979 Temperature field measurement of an axisymmetric laminar plume. *Phys. Fluids* **22**, 631–634.
SHLIEN, D.J. & THOMPSON, D.W. 1975 Some experiments on the motion of an isolated laminar thermal. *J. Fluid Mech.* **72**, 35–47.
SILANO, G., SREENIVASAN, K.R. & VERZICCO, R. 2010 Numerical simulations of Rayleigh–Bénard convection for Prandtl numbers between 10^{-1} and 10^4 and Rayleigh numbers between 10^5 and 10^9. *J. Fluid Mech.* **662**, 409–446.
SPARKS, R.S.J. 1986 The dimensions and dynamics of volcanic eruption columns. *Bull. Volcanol.* **48**, 3–15.
STOTHERS, R.B. 1989 Turbulent atmospheric plumes above line sources with an application to volcanic fissure eruptions on the terrestrial planets. *J. Atmos. Sci.* **46**, 2662–2670.
SUN, C. & XIA, K.-Q. 2007 Multi-point local temperature measurements inside the conducting plates in turbulent thermal convection. *J. Fluid Mech.* **570**, 479–489.
TURNER, J.S. 1962 The 'starting plume' in neutral surroundings. *J. Fluid Mech.* **13**, 356–368.
TURNER, J.S. 1969 Buoyant plumes and thermals. *Annu. Rev. Fluid Mech.* **1**, 29–44.
TURNER, J.S. 1973 *Buoyancy Effects in Fluids*. Cambridge University Press.
VEST, C.M. & LAWSON, M.L. 1972 Onset of convection near a suddenly heated horizontal wire. *Intl J. Heat Mass Transfer* **15**, 1281–1283.
WANG, Y., XU, W., HE, X., YIK, H., WANG, X., SCHUMACHER, J. & TONG, P. 2018 Boundary layer fluctuations in turbulent Rayleigh–Bénard convection. *J. Fluid Mech.* **840**, 408–431.
WHITTAKER, R.J. & LISTER, J.R. 2008 The self-similar rise of a buoyant thermal in very viscous flow. *J. Fluid Mech.* **606**, 295–324.
WILSON, L., SPARKS, R.S.J., HUANG, T.C. & WATKINS, N.D. 1978 The control of volcanic column heights by eruption energetics and dynamics. *J. Geophys. Res.* **83**, 1829–1836.
WOODS, A.W. 2010 Turbulent plumes in nature. *Annu. Rev. Fluid Mech.* **42**, 391–412.
WORSTER, M.G. 1986 The axisymmetric laminar plume: asymptotic solution for large Prandtl number. *Stud. Appl. Maths* **75**, 139–152.

XI, H.-D., LAM, S. & XIA, K.-Q. 2004 From laminar plumes to organized flows: the onset of large-scale circulation in turbulent thermal convection. *J. Fluid Mech.* **503**, 47–56.

XU, W., WANG, Y., HE, X., WANG, X., SCHUMACHER, J., HUANG, S.-D. & TONG, P. 2021 Mean velocity and temperature profiles in turbulent Rayleigh–Bénard convection at low Prandtl numbers. *J. Fluid Mech.* **918**, A1.

YIH, C.S. 1952 Laminar free convection due to a line source of heat. *Trans. Am. Geophys. Union* **33**, 669–672.

ZHOU, Q., STEVENS, R.J.A.M., SUGIYAMA, K., GROSSMANN, S., LOHSE, D. & XIA, K.-Q. 2010 Prandtl–Blasius temperature and velocity boundary-layer profiles in turbulent Rayleigh–Bénard convection. *J. Fluid Mech.* **664**, 297–312.

ZHOU, S.Q., XIE, Y.C., SUN, C. & XIA, K.-Q. 2016 Statistical characterization of thermal plumes in turbulent thermal convection. *Phys. Rev. Fluids* **1**, 054301.